Electronic Supplementary Material (ESI) for Catalysis Science & Technology.

Supporting Information

Comprehensive Insights into Coverage-affected Selective Catalytic Oxidation of Ethylene on Ag(111) from Microkinetical Analyses

Zhuozheng Wang,[1] Wenbo Xie,[1] Yarong Xu,[1,2] Menglei Jia,[1,3] Jiayan Xu,[1] P. Hu[1,3]*

[1]School of Chemistry and Chemical Engineering, The Queen's University of Belfast, Belfast BT9 5AG, United Kingdom

[2]Research Institute of Urumqi Petrochemical Company, Petrochina Company Limited, Urumqi 830019, China

[3]Key Laboratory for Advanced Materials, Centre for Computational Chemistry and Research Institute of Industrial Catalysis, East China University of Science and Technology, 130 Meilong Road, Shanghai 200237, China

Contents

S1. Details of surfaces species during the reaction.

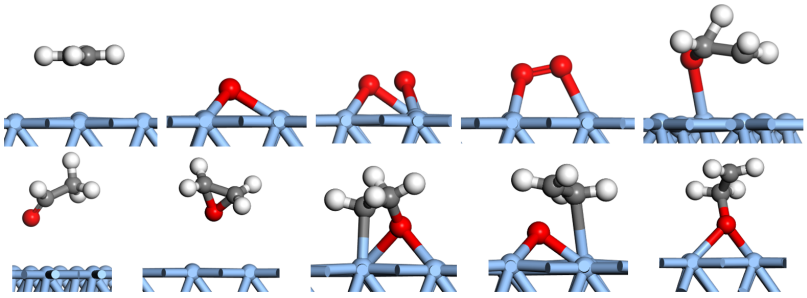

Figure S1 Side view of surfaces species. The first row (from left to right): C_2H_4*, O*, O_2**, TSOO, and TSAA. The second row (from left to right): AA*, EO*, OME*, TS1, and TSEO. Color code: red, oxygen; white, hydrogen; dark grey, carbon; blue, silver.

S2. Structures of adsorbates and transition state at different coverages.

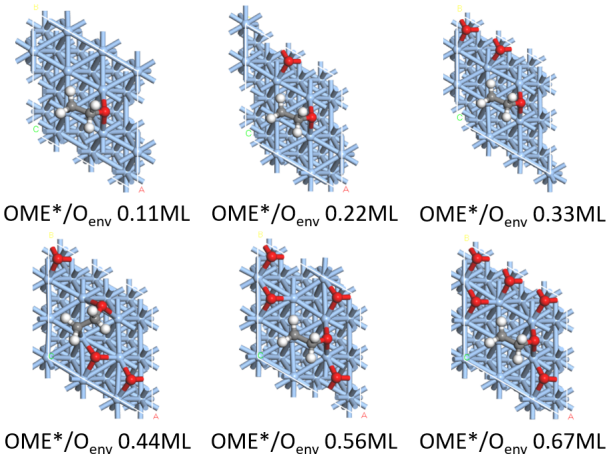

Figure S2 Structures of OME*/O_{env} at the coverage from 0.11 ML to 0.67 ML. The color coding is the same as in **Figure S1**.

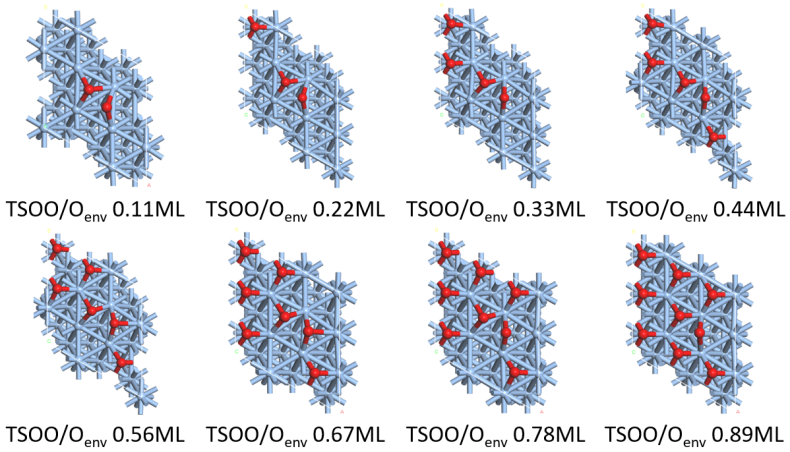

Figure S3 Structures of TSOO/O$_{env}$ at the coverage from 0.11 ML to 0.89 ML.

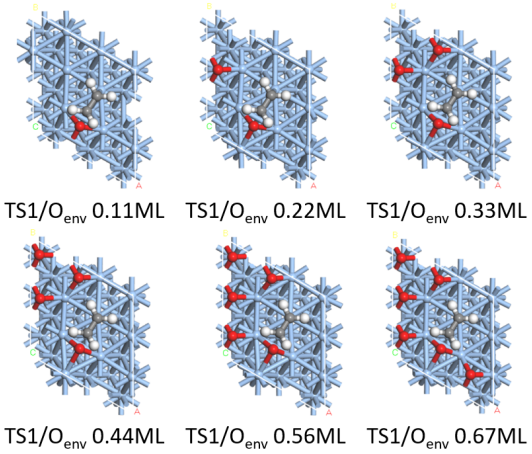

Figure S4 Structures of TS1/O$_{env}$ at the coverage from 0.11 ML to 0.67 ML.

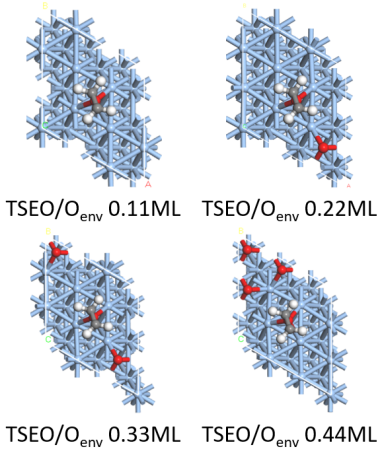

Figure S5 Structures of TSEO/O$_{env}$ at the coverage from 0.11 ML to 0.44 ML.

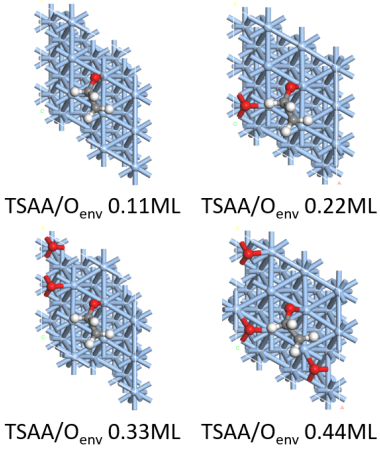

Figure S6 Structures of TSAA/O$_{env}$ at the coverage from 0.11 ML to 0.44 ML.

S3. Coverage-dependent diagrams of adsorption energy related to coverage.

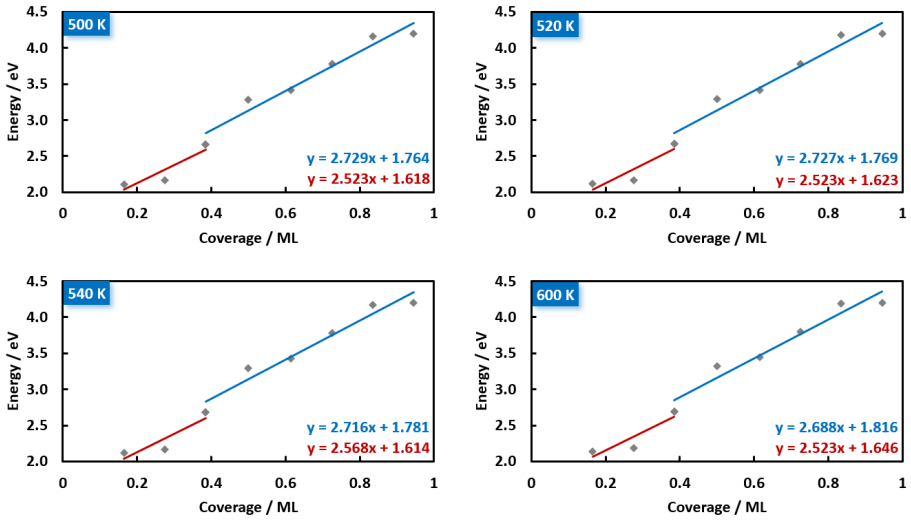

Figure S7 Variations of O*/O$_{env}$ adsorption free energies with different coverages at 500 K, 520 K, 540 K, and 600 K. The red lines represent the linear curves at low coverages, and the blue lines represent the linear curves at high coverages.

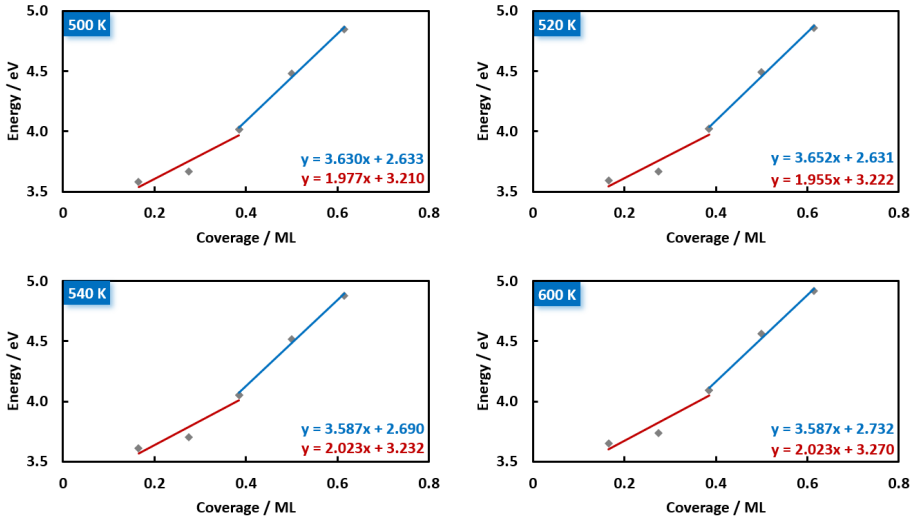

Figure S8 Variations of OME*/O_{env} adsorption free energies with different coverages at 500 K, 520 K, 540 K, and 600 K. The color coding is the same as in **Figure S7**.

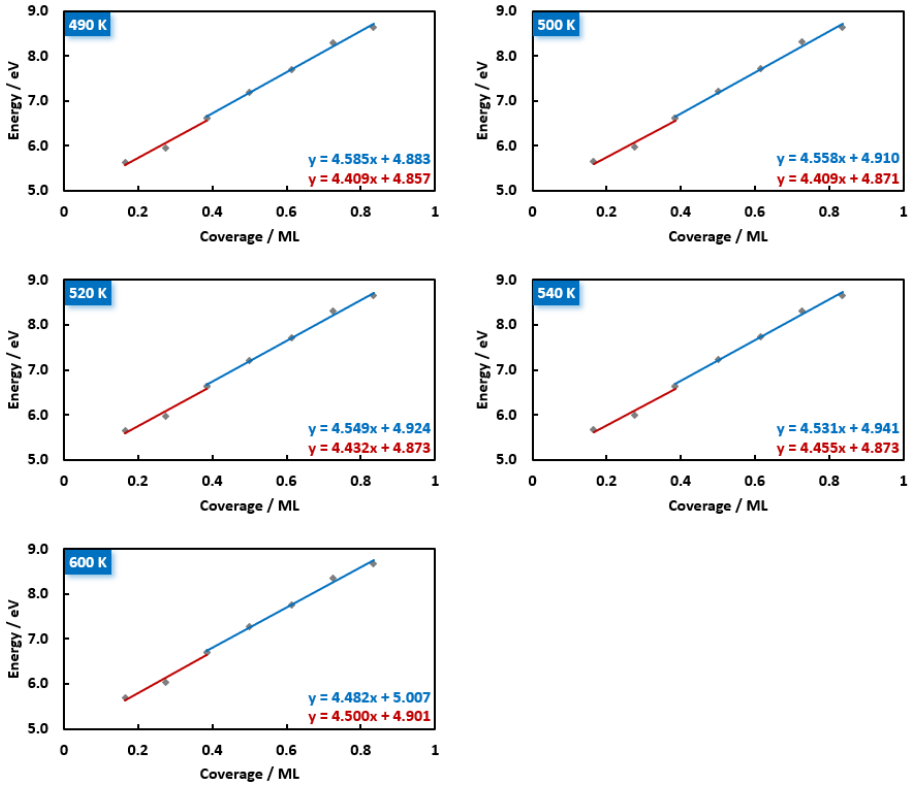

Figure S9 Variations of TSOO/O_{env} adsorption free energies with different coverages at 490 K, 500 K, 520 K, 540 K, and 600 K.

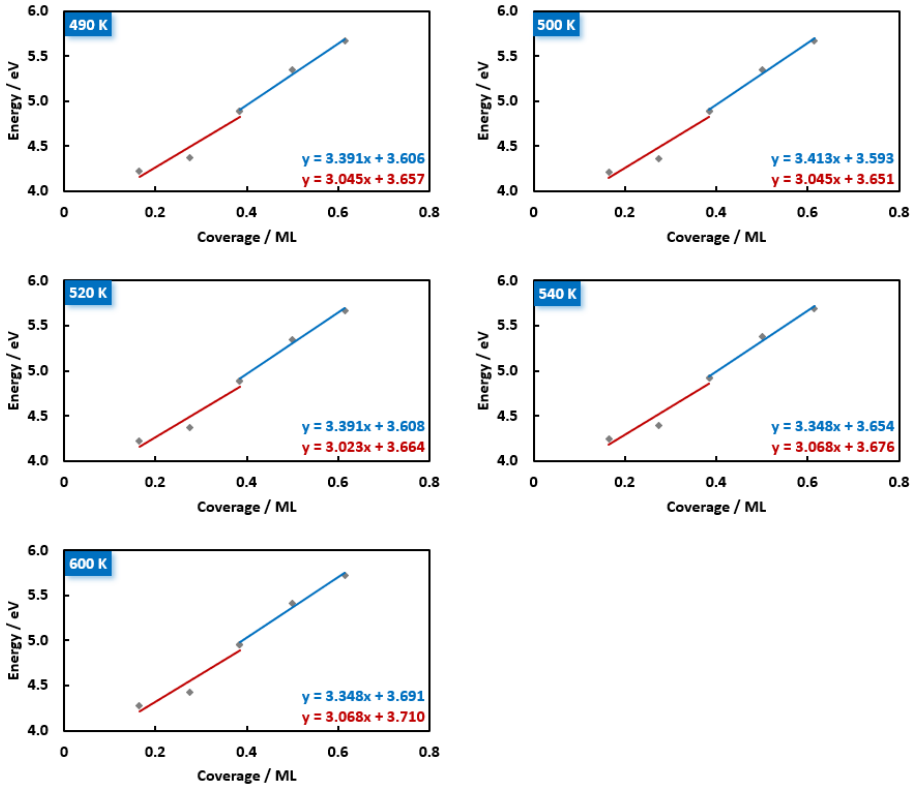

Figure S10 Variations of TS1/O_{env} adsorption free energies with different coverages at 490 K, 500 K, 520 K, 540 K, and 600 K.

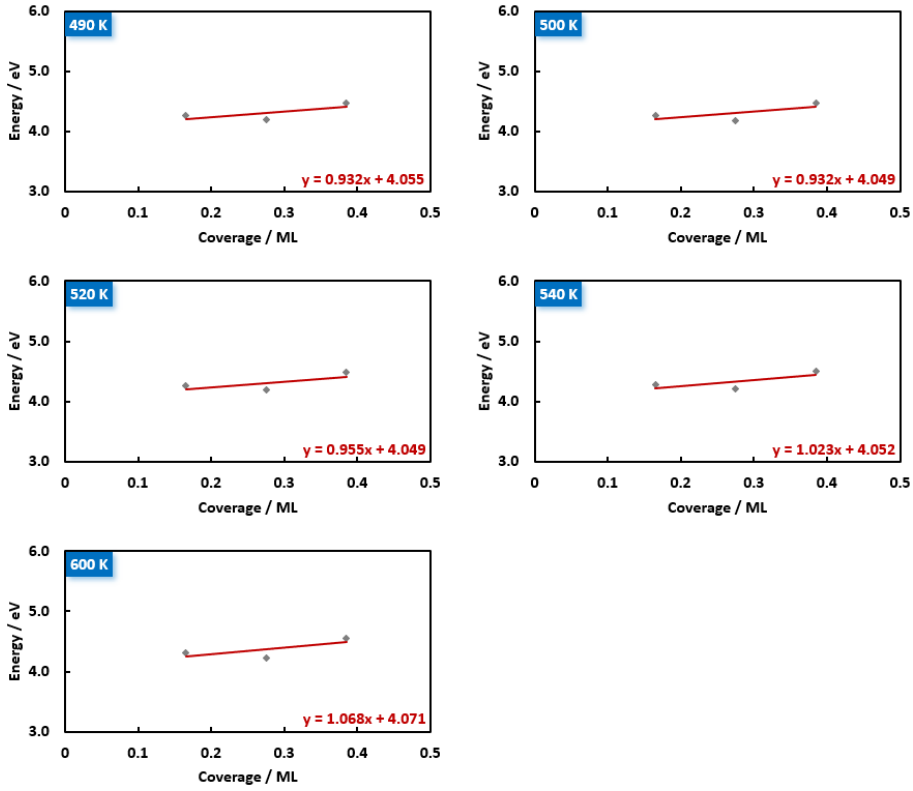

Figure S11 Variations of TSEO/O_{env} adsorption free energies with different coverages at 490 K, 500 K, 520 K, 540 K, and 600 K.

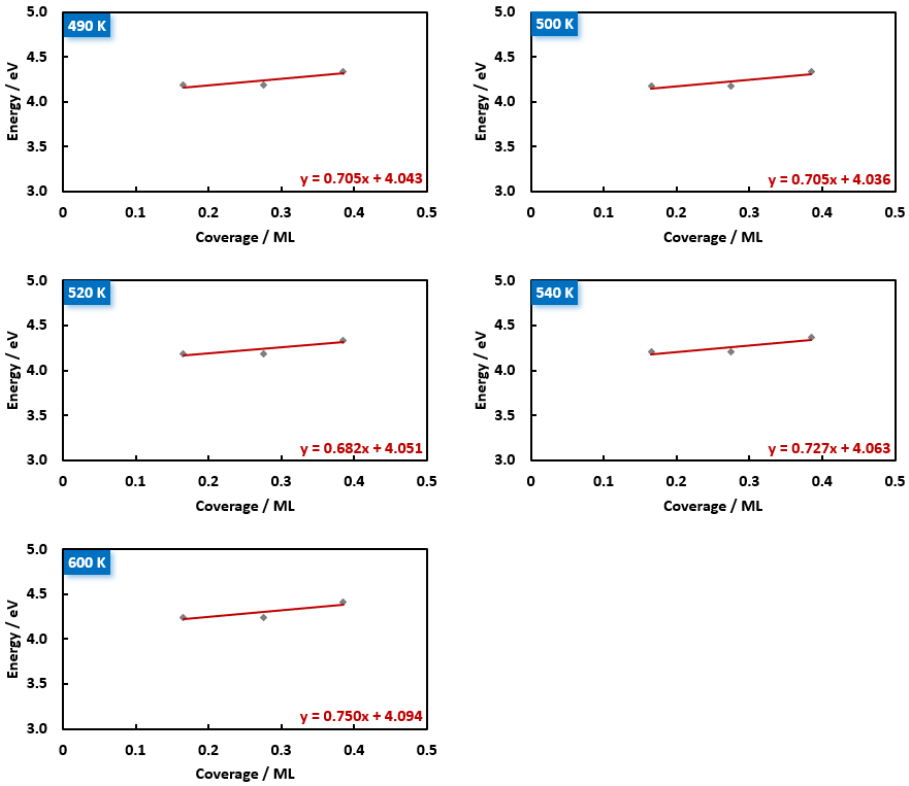

Figure S12 Variations of TSAA/O_{env} adsorption free energies with different coverages at 490 K, 500 K, 520 K, 540 K, and 600 K.

S4. Additional Gibbs free energy profiles.

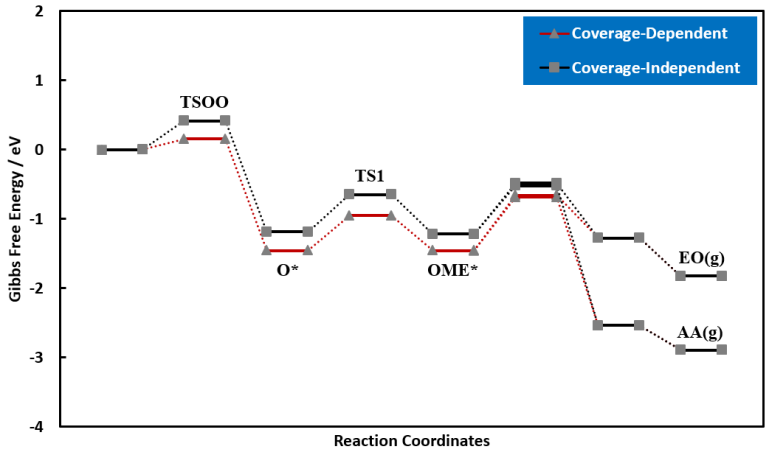

Figure S13 Free energy profiles of ethylene epoxidation on Ag(111) with E-R mechanism at 490 K, $P_{O_2} = P_{Et} = 13.4$ kPa. Note that there are regions in which the two profiles overlap with each other.

S5. Formation energies

Parameterizing the classical energies reduces errors in the simulations and ensures thermodynamic consistency for an intricate surface reaction like ethylene epoxidation. The generalized formation energies and corresponding energies of species, which are thoroughly exploited and skillfully applied,[1] could be rigorously applied to the ethylene epoxidation system in this work:

$$\begin{aligned} R_H &= \frac{1}{2}\left(U_{H_2}\right) \\ R_C &= U_{CH_4} - 4R_H \\ R_O &= U_{H_2O} - 2R_H \end{aligned} \tag{S1}$$

The calculation expressions for the formation energies of all participating species are illustrated in **Table S1**, where E represents the generalized formation energy, U is the free energy calculated by DFT, and R indicates the reference atomic species.

Table S1 List of all species involved in the reaction and corresponding formation energy calculation expressions.

Species	Calculation Expressions
C_2H_4 (gas)	$E_{C_2H_4} = U_{C_2H_4} - 2R_C - 4R_H$
O_2 (gas)	$E_{O_2} = U_{O_2} - 2R_O$
EO (gas)	$E_{EO} = U_{EO} - 2R_C - 4R_H - R_O$
AA (gas)	$E_{AA} = U_{AA} - 2R_C - 4R_H - R_O$
C_2H_4*	$E_{C_2H_4*} = U_{C_2H_4(surface)} - U_{(surface)} - 2R_C - 4R_H$
O*	$E_{O*} = U_{O(surface)} - U_{(surface)} - R_O$

O_2*	$E_{O_2*} = U_{O_2(surface)} - U_{(surface)} - 2R_O$
EO*	$E_{EO*} = U_{EO(surface)} - U_{(surface)} - 2R_C - 4R_H - R_O$
AA*	$E_{AA*} = U_{AA(surface)} - U_{(surface)} - 2R_C - 4R_H - R_O$
OME*	$E_{OME*} = U_{OME(surface)} - U_{(surface)} - 2R_C - 4R_H - R_O$
TSOO	$E_{TSOO*} = U_{TSOO(surface)} - U_{(surface)} - 2R_O$
TS1	$E_{TS1*} = U_{TS1(surface)} - U_{(surface)} - 2R_C - 4R_H - R_O$
TSEO	$E_{TSEO*} = U_{TSEO(surface)} - U_{(surface)} - 2R_C - 4R_H - R_O$
TSAA	$E_{TSAA*} = U_{TSAA(surface)} - U_{(surface)} - 2R_C - 4R_H - R_O$

The calculation expressions for the formation energies of all participating species are illustrated in **Table S1**, where *E* represents the generalized formation energy, *U* is the free energy

S6. Thermodynamic Corrections

The thermodynamic corrections from DFT-based vibrational frequencies for obtaining free energies were applied on all the adsorption and transition states with different surface coverages. The vibrational frequencies were calculated with each targeted surface species being relaxed and all the environmental adsorbates and the surface being fixed. All the zero-point energy corrections were included. The zero-point energy (ZPE) correction was calculated as follows:

$$ZPE = \sum_i \frac{h\nu_i}{2} \tag{S2}$$

where ν_i is the vibrational frequency calculated utilizing the harmonic oscillator approximation and h is the Plank's constant. The standard thermal energy contribution is calculated as

$$U = RT \sum_i \frac{h\nu_i / k_B}{e^{h\nu_i / k_B T} - 1} \tag{S3}$$

where R is the gas constant, and k_B is the Boltzmann's constant. The standard vibrational

entropy is calculated by

$$S = R\sum_i \left[\frac{h\nu_i / k_B}{e^{h\nu_i / k_B T} - 1} - \ln\left(1 - e^{-\frac{h\nu_i}{k_B T}}\right) \right] \quad \text{(S4)}$$

The standard Gibbs free energy can be attained by summing up the thermodynamic corrections of zero-point-energy (ZPE), thermal energy (U) and entropy (S) derived from the vibrational partition function as follows:

$$\Delta G_{ad} = E_{ad} + \Delta ZPE + \Delta U - T\Delta S \quad \text{(S5)}$$

where E_{ad} is the adsorption energy from DFT total energy calculations. All the transition states were confirmed by the vibrational frequency analysis.

S7. Determination of the lowest energy structure

We optimized all the possible configurations for each surface species, including O*, OME*, TSOO, TS1, TSEO, and TSAA, under each coverage. In each case, all the configurations we could think of were tried. Then the structure with the lowest energy was selected as the corresponding structure to determine the energy for our kinetic simulations. Taking TS1/O_{env} as an example, at 0.33 ML, eight different TS configurations were calculated (**Figure S14**). The lowest energy structure was obtained from the configuration set of 0.33 ML, which was selected for the kinetic simulation at 0.33 ML.

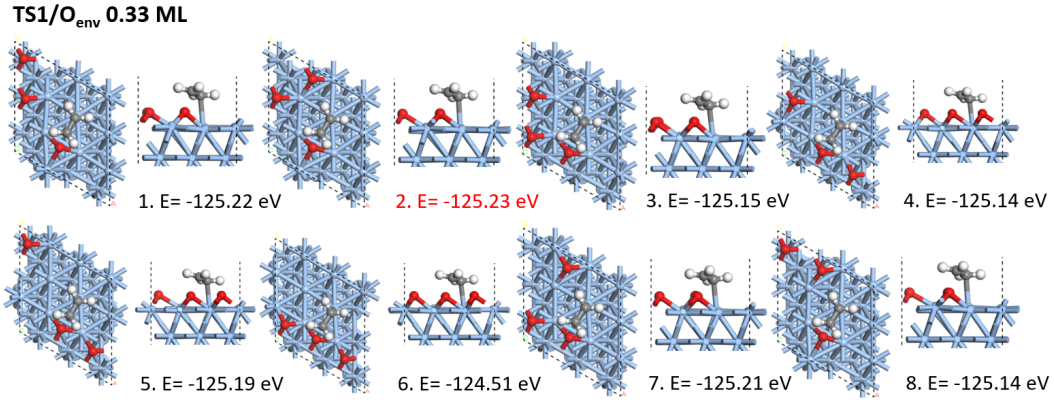

Figure S14 All possible surface TS structures at 0.33 ML in TS1/O_{env}. The red mark indicates the lowest energy structure.

S8. The Mean-field approximation

A mean-field approximation was used in in our work. It is worth noting that the mean-field approximation has been widely utilized in all the microkinetic simulations and has shown its effectiveness in heterogeneous catalysis: It is reasonably accurate but not very computational demanding. Some examples can be seen in **Table S2** below.

Table S2 Experiments versus the mean-field microkinetic model predictions in different catalytic reaction systems.

	Experimental TOF(s^{-1})	**Mean-field microkinetic model predicted TOF(s^{-1})**
CO oxidation on Rh(111)[2]	560	820
C2H2 hydrogenation on Pd(111)[3]	2.66	1.41
1,2-Dichloroethane hydrodechlorination on Pt/SiO_2[4]	0.011	0.009

As shown in **Table S2**, the mean-field approximation in kinetic simulations is a good approximation. There are good reasons for the accuracy of the mean-field approximation in this system: (i) Typically, surface species adsorb randomly on the surface; (ii) the interactions of surface species are commonly repulsive; and (iii) many reaction temperatures are relatively high. These factors ensure relatively uniform distributions of surface species on the surfaces.

S9. Analysis of apparent activation energy and reaction order

The apparent activation energy and reaction order are two important properties in reaction kinetics. We calculated the apparent activation barrier that is 13.2 kJ/mol, which is lower than that of the experimental one (42.9 kJ/mol). We guess that the reason for the considerable difference may be the following: There are still some errors in our computational work, such as functional in DFT. It is worth noting that our work represents one of the most accurate kinetic results from theoretical simulations without any experimental input.

Regarding the reaction orders, we used the following two approaches. (i) Analytical approach: Our kinetic simulations show that the rate determining step is the O_2 dissociation, the rate of which is defined as rate(O_2). Hence, according to the principle of kinetics, the total rate can be approximated as rate(O_2). Because rate(O_2) = k(p_{O_2}), the reaction orders are zero order in C_2H_4 and first order in O_2. (ii) Numerical approach: Our numerical analysis from the kinetic simulations suggests that the reaction order is 0.09 in C_2H_4 and 0.91 in O_2. It is clear that both approaches give rise to the consistent reaction orders. In **Table S3**, we list some relevant experimental results. It can be seen that the reaction orders from our theoretical simulations without any experimental parameters are largely consistent with the experimental works.

Table S3 Some information for ethylene epoxidation on silver catalysts. The last two columns are reaction orders.

Authors	Catalyst	Reaction conditions	n(C_2H_4)	n(O_2)
Kenson and Lapkin (1970)[5]	10 wt % Ag/Al_2O_3	3.44 bar, 55% C_2H_4, 45% air, 453−513 K	0	1
Force and Bell (1975)[6]	6.6 wt % Ag/Cab-O-Sil M5	0.055−0.182 bar C_2H_4, 0.156−0.390 bar O_2 443−493 K	1	0.5
Dettwiler et al. (1979)[7]	8 wt % Ag/pumice	0.002−0.03 bar C_2H_4, 0.05−0.2 bar O_2, 493−623 K	1	0.5
Jankowiak and Barteau (2005)[8]	Ag (11−13 wt %)/α-Al_2O_3	1.36 bar, 10−60% C_2H_4, 10−60% O_2, 500−540 K	0.19	0.65
Jankowiak and Barteau (2005)[8]	Ag (11−13 wt %), Cu (0.5 mol %)/α-Al_2O_3	1.36 bar, 10−60% C_2H_4, 10−60% O_2, 500−540 K	0.2	0.48
Chen et al. (2018)[9]	Ag (35 wt %)/α-Al_2O_3 Cs (628 ppm), Li (33 ppm), Na (42 ppm), Re (440 ppm), $[SO_4]^{2-}$ (151 ppm), Mn (115 ppm)	5.3 bar, 20−40% C_2H_4, 2−7% O_2, 0.4% C_2H_6, 1% CO_2, 1.5 ppm of C_2H_5Cl, 508−523 K	0.5	0.7
Chen et al. (2018)[9]	Same as above	5.3 bar, 20−40% C_2H_4, 2−7% O_2, 0.4% C_2H_6, 1% CO_2, 6.3 ppm of C_2H_5Cl, 508−523 K	-0.4	1

S10. The influence of van der Waals interaction

As demonstrated by our work, the coverage effect is important. Test functionals in DFT, we constructed a set of DFT energetics without van der Waals corrections. Then we performed the microkinetic simulation using the DFT energetics without van der Waals corrections with p_{O_2} = 20 kPa and p_{Et} = 2.66 kPa. The results are shown in **Figure S15**. It can be seen from **Figure**

S15 that the coverage-dependent model with the energetics without DFT-D3 correction give rise to the results that are not consistent with the experimental values. The most distorted results are the coverage-independent ones without DFT-D3 correction; the TOF values are far away from the experimental ones.

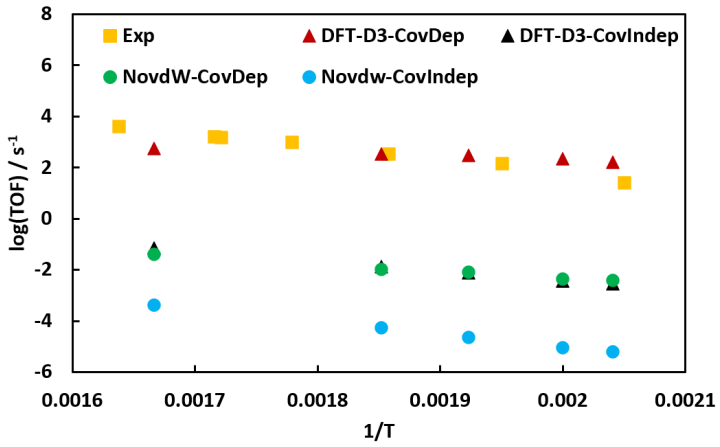

Figure S15 Comparison among the experimental data from Campbell,[10] simulated values obtained from the coverage-dependent/coverage-independent microkinetic modellings with and without DFT-D3 corrections at p_{O_2} = 20 kPa and p_{Et} = 2.66 kPa. Experimental data: yellow square; coverage dependent results with DFT-D3 corrections: red triangle; coverage independent results with DFT-D3 corrections: black triangle; coverage dependent results without DFT-D3 corrections: green circle; coverage independent results without DFT-D3 corrections: blue circle.

S11. Degree of rate control (DRC) analysis of ethylene epoxidation based on coverage-dependent microkinetic modelling

In order to study the rate-determining step on the selectivity of the reaction system, the concept of degree of rate control (DRC) defined by Campbell was adopted herein.[11,12] The DRC represents the impact of each elementary step on the overall reaction rate, which can be expressed as:

$$DRC_i = \left(\frac{\partial \ln r}{\partial \ln k_i}\right)_{k_{j\neq i},K_i} = \frac{k_i}{r}\left(\frac{\partial r}{\partial k_i}\right)_{k_{j\neq i},K_i} \quad \text{(S6)}$$

where r is the net reaction rate of the target species, k_i is the rate constant of elementary step i, and K_i is the corresponding equilibrium constant. DRC_i is a quantitative measure of the impact of step i on the total rate. In this work, the selective competition steps were chosen for DRC analysis, namely OME* → EO* (step 6) and OME* → AA* (step 7), as shown in **Figure S16**.

Firstly, the coverage-dependent microkinetic modelling was performed to analyze the EO formation and the DRC results are illustrated in **Figure S16** (a). Three elementary steps that have the most significant impacts on the EO formation reaction rate were found: oxygen dissociation (O_2** → 2O*, step 3) and the selective competition reactions (OME* → EO*, step 6; OME* → AA*, step 7). With the temperature changes, the DRC of step 3 and step 6 are always positive, indicating that the reaction rate of the EO pathway (step 6) will increase if the reaction barriers of these two steps decrease. By contrast, the DRC of step 7 is negative, suggesting that the decrease of the barrier for step 7 would slow down step 6. The DRC signal of step 6 and step 7 is distinctly opposite, which can be explained by the selective branching from the oxametallacycle. When the temperature increases from 490 K to 600 K, the DRC values of the step 6 moderately decline from 0.68 to 0.52, while the DRC of the step 7 gradually rises from -0.57 to -0.43. Both the absolute DRC values of steps 6 and 7 become smaller, indicating that as the temperature rises, the reaction barrier changes of the selective competition steps in ethylene epoxidation have a diminished effect on the EO pathway.

The DRC analysis of the AA formation pathway (step 7) from the coverage-dependent microkinetic modelling was also performed, as shown in **Figure S16** (b). As one of the selective competition steps, the AA pathway acts as the inhibitory reaction to the EO pathway. Therefore, the DRC signs of the step 6 and step 7 are opposite to the corresponding ones in the EO pathway. In addition, it is interesting to note that the temperature-related DRC trend that affects the AA pathway is opposed to the EO pathway. As the temperature increases, the DRC of step 6 drops from -0.32 to -0.48, while the DRC value of step 7 increases from 0.43 to 0.57. It means that the influence of the AA formation reaction barrier change on the reaction rate is significantly enhanced with the increase of temperature.

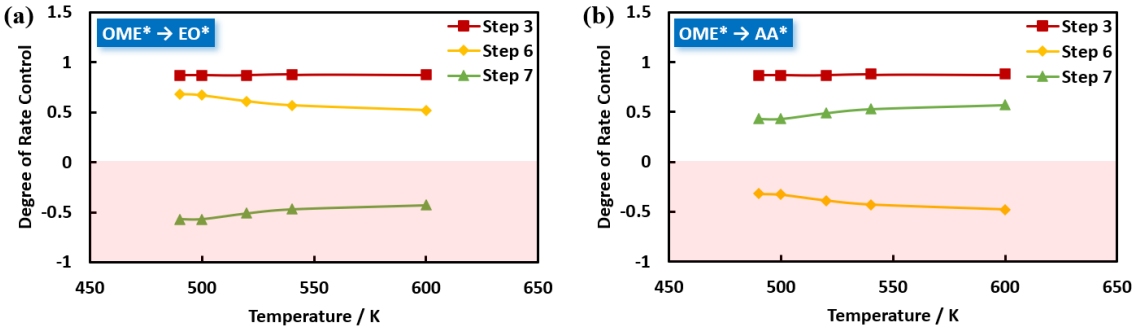

Figure S16 DRC analysis for the selective competition steps: (a) OME* → EO* and (b) OME* → AA* from 490 K to 600 K with p_{O_2}/p_{Et} = 1:1.

Regarding the promotion effect on the selective competition steps, it is interesting to notice that the DRC value of step 6 (0.68 to 0.52, **Figure S16** (a)) decreases generally and finally becomes smaller than that of step 7 (0.43 to 0.57, **Figure S16** (b)) from 490 K to 600 K. As for the inhibiting effect on the selective competition steps, the absolute DRC value of step 7 (-0.57 to -0.43 in **Figure S16** (a)) reduces gradually and is finally smaller than that of step 6 (-0.32 to -0.48, **Figure S16** (b)) as well. Taken together, these results indicate that the AA formation rate is easier to be influenced than the EO formation rate by the temperature increase. Interestingly, the impact of oxygen dissociation (step 3) always remains positive and identical in both EO formation DRC and AA formation DRC, as shown in **Figure S16**.

References

1 A. J. Medford, C. Shi, M. J. Hoffmann, A. C. Lausche, S. R. Fitzgibbon, T. Bligaard and J. K. Nørskov, *Catal. Letters*, 2015, **145**, 794–807.

2 C. Guo, Y. Mao, Z. Yao, J. Chen and P. Hu, *J. Catal.*, 2019, **379**, 52–59.

3 W. Xie, J. Xu, Y. Ding and P. Hu, *ACS Catal.*, 2021, **11**, 4094–4106.

4 L. Xu, E. E. Stangland, J. A. Dumesic and M. Mavrikakis, *ACS Catal.*, 2021, **11**, 7890–7905.

5 R. E. Kenson and M. Lapkin, *J. Phys. Chem.*, 1970, **74**, 1493–1502.

6 E. L. Force and A. T. Bell, *J. Catal.*, 1975, **40**, 356–371.

7 H. R. Dettwiler, A. Baiker and W. Richarz, *Helv. Chim. Acta*, 1979, **62**, 1689–1700.

8 J. T. Jankowiak and M. A. Barteau, *J. Catal.*, 2005, **236**, 366–378.

9 C. J. Chen, J. W. Harris and A. Bhan, *Chem. - A Eur. J.*, 2018, **24**, 12405–12415.

10 C. T. Campbell, *J. Catal.*, 1985, **94**, 436–444.

11 C. T. Campbell, *Top. Catal.*, 1994, **1**, 353–366.

12 C. T. Campbell, *ACS Catal.*, 2017, **7**, 2770–2779.